Nanoscale

Electronic state modulation of Ag_{30} nanoclusters within a ring-shaped polyoxometalate

Journal:	*Nanoscale*
Manuscript ID	NR-ART-06-2024-002547.R2
Article Type:	Paper
Date Submitted by the Author:	22-Aug-2024
Complete List of Authors:	Yanai, Daiki; Tokyo Daigaku - Hongo Campus, Department of Applied Chemistry, School of Engineering, Yonesato, Kentaro; The University of Tokyo, Department of Applied Chemistry, School of Engineering, Kikkawa, Soichi ; Tokyo Metropolitan University - Minamiosawa Campus, Yamazoe, Seiji; Tokyo Metropolitan University, Department of Chemistry Yamaguchi, Kazuya; The University of Tokyo, Applied Chemistry Suzuki, Kosuke; The University of Tokyo, Department of Applied Chemistry, School of Engineering,

Nanoscale

ARTICLE

Electronic state modulation of Ag_{30} nanoclusters within a ring-shaped polyoxometalate

Daiki Yanai,[a] Kentaro Yonesato,*[a] Soichi Kikkawa,[b] Seiji Yamazoe,[b] Kazuya Yamaguchi,[a] and Kosuke Suzuki *[a]

Received 00th January 20xx,
Accepted 00th January 20xx

DOI: 10.1039/x0xx00000x

Atomically precise Ag nanoclusters display distinctive properties that are dictated by their structures and electronic states. However, manipulating the electronic states of Ag nanoclusters is challenging owing to their inherent instability and susceptibility to undesired structural changes, decomposition, and aggregation. Recently, we reported the synthesis of a body-centered cubic $\{Ag_{30}\}^{22+}$ nanocluster encapsulated within a ring-shaped polyoxometalate (POM) $[P_8W_{48}O_{184}]^{40-}$ by reacting 16 Ag^+-containing $[P_8W_{48}O_{184}]^{40-}$ with Ag^+ using *N*,*N*-dimethylformamide (DMF) as a mild reducing agent. This led to a redox-induced structural transformation into a face-centered cubic $\{Ag_{30}\}^{16+}$ nanocluster. In this study, we demonstrated the modulation of the electronic states of Ag_{30} nanoclusters within the ring-shaped POM through two different approaches. A face-centered cubic $\{Ag_{30}\}^{18+}$ nanocluster, featuring distinct oxidation states compared to previously reported $\{Ag_{30}\}^{22+}$ and $\{Ag_{30}\}^{16+}$ nanoclusters, was synthesized using tetra-*n*-butylammonium borohydride, a stronger reducing agent than DMF, in the reaction of 16 Ag^+-containing $[P_8W_{48}O_{184}]^{40-}$ and Ag^+. Additionally, by leveraging the acid–base properties of POMs, we demonstrated the reversible, stepwise modulation of the charge distribution in the Ag_{30} nanocluster through controlling protonation states of the ring-shaped POM ligand. These results highlight the potential of engineering POM-stabilized Ag nanoclusters with diverse structures and electronic states, thereby facilitating the exploration of novel properties and applications utilizing the unique characteristics of the POM ligands.

Introduction

Atomically precise metal nanoclusters of group 10 and 11 elements, such as Au, Ag, Cu, Pd, and Pt, have attracted increasing interest in various fields, including catalysis, magnetic devices, pharmaceuticals, optical materials, and sensors.[1] This interest stems from their unique properties, which are intrinsically linked to their structures and electronic states. To date, substantial advancements in the synthesis of metal nanoclusters have enabled extensive structural tuning of their constituent metal elements, stabilizing ligands, and sizes, leading to the successful construction of these metal nanoclusters.

Recent studies on Au and Au-alloy nanoclusters, particularly $[Au_{25}(SR)_{18}]^q$ nanoclusters (where q = −1, 0, and +1),[2] have highlighted the profound effect of their oxidation states on the physicochemical properties of metal nanoclusters. These properties include stability,[3] magnetic characteristics,[4] optical behaviors,[5] and catalytic activity.[6] Moreover, metal nanoclusters with identical structures and oxidation states exhibit varying physicochemical properties influenced by the electron-donating abilities of stabilizing ligands.[7] These studies highlight the importance of controlling metal nanoclusters' electronic states, including oxidation states and electron donation from stabilizing ligands, to develop novel properties and applications. However, modifying the electronic states of metal nanoclusters is typically difficult, and often leads to undesirable aggregation or decomposition. In particular, Ag nanoclusters are generally unstable and prone to structural changes, limiting the successful modification of their electronic states to only a few reports.[8]

Polyoxometalates (POMs) are anionic metal oxide clusters known for their diverse, well-defined structures and unique properties, including acid–base, redox, and optical characteristics.[9] POMs have been employed as attractive inorganic ligands for Ag nanoclusters owing to their oxygen-enriched molecular surfaces and variable properties.[10,11] Recently, we developed a synthetic method for Ag nanoclusters stabilized by lacunary POMs. These act as inorganic multidentate ligands with highly reactive oxygen atoms at vacant sites.[12,13] In particular, using a ring-shaped POM $[P_8W_{48}O_{184}]^{40-}$ (**P8W48**), consisting of a tetramer of hexavacant lacunary Dawson-type $\{P_2W_{12}\}$ units,[14,15] we synthesized surface-exposed Ag_{30} nanoclusters via a stepwise reduction method (Figs. 1, S1a).[13] The reaction involving 16 Ag^+-containing **P8W48** ($[Ag_{16}P_8W_{48}O_{184}]^{24-}$, denoted as **Ag16**) and additional Ag^+ in *N*,*N*-dimethylformamide (DMF), acting as

[a] *Department of Applied Chemistry, School of Engineering, The University of Tokyo, 7-3-1 Hongo, Bunkyo-ku, Tokyo 113-8656, Japan. E-mail: ksuzuki@appchem.t.u-tokyo.ac.jp; k-yonesato@g.ecc.u-tokyo.ac.jp*
[b] *Department of Chemistry, Graduate School of Science, Tokyo Metropolitan University, 1-1 Minami Osawa, Hachioji, Tokyo 192-0397, Japan.*
†Electronic Supplementary Information (ESI) available: Experimental details, Table S1–S7 and Figs. S1–S16. See DOI: 10.1039/x0xx00000x

a mild reducing agent, led to the formation of an $\{Ag_{30}\}^{22+}$ nanocluster within **P8W48** (denoted as **Ag30**). This $\{Ag_{30}\}^{22+}$ nanocluster underwent further reduction upon reaction with tetra-*n*-butylammonium borohydride ($TBABH_4$), resulting in an $\{Ag_{30}\}^{16+}$ nanocluster (denoted as **I**). Importantly, **P8W48** served as an effective stabilizing ligand for Ag nanoclusters with varying structures and oxidation states: the $\{Ag_{30}\}^{22+}$ nanocluster featured a body-centered cubic (bcc) atom arrangement. In contrast, the $\{Ag_{30}\}^{16+}$ nanocluster exhibited a face-centered cubic (fcc) atom arrangement. Consequently, we expected that **P8W48** could facilitate the formation of Ag nanoclusters with diverse electronic states, thus driving the advancement of novel applications for POM-stabilized Ag nanoclusters.

In this study, we demonstrated the modulation of electronic states in Ag_{30} nanoclusters within a ring-shaped POM through two distinct approaches (Fig. 1): (a) oxidation-state modulation by changing the synthetic conditions and (b) charge-distribution modulation by changing the protonation states of **P8W48**. Specifically, we synthesized an $\{Ag_{30}\}^{18+}$ nanocluster (**II**) within **P8W48** using a strong reducing reagent ($TBABH_4$) in a reaction involving **Ag16** and Ag^+ ions. The $\{Ag_{30}\}^{18+}$ nanocluster in **II** exhibited structural similarity to the $\{Ag_{30}\}^{16+}$ nanocluster in **I**, maintaining an fcc metal arrangement despite the different oxidation states. Subsequently, by leveraging the acid–base properties of POMs, we demonstrated the ability to reversibly and stepwise control the charge distribution of Ag_{30} nanoclusters in **II** through the process of protonation and deprotonation of **P8W48**. These findings demonstrate that the electronic states of POM-stabilized Ag nanoclusters can be manipulated through synthetic conditions and post-synthetic modulation via protonation states. This capability will expedite the advancement of their applications across diverse fields.

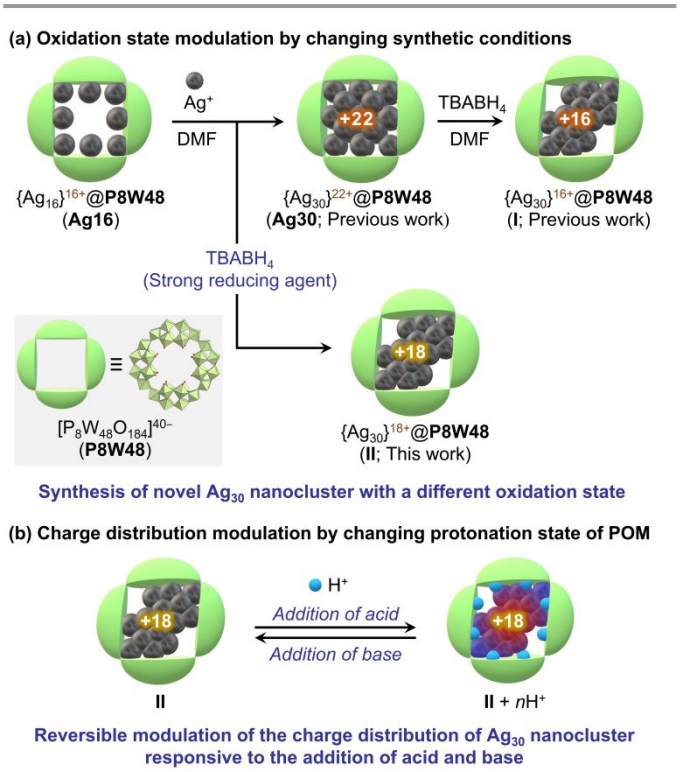

Fig. 1 Diagram illustrating the modulation of electronic states in Ag_{30} nanoclusters within a ring-shaped POM. (a) Modulation of oxidation states in Ag_{30} nanoclusters through variations in synthetic conditions. (b) Modulation of charge distribution via protonation and deprotonation of the ring-shaped POM.

Results and discussion

The $\{Ag_{30}\}^{22+}$ nanocluster within **P8W48** (i.e., **Ag30**) was synthesized by reacting 16 Ag^+-containing **P8W48** (i.e., **Ag16**) with silver acetate in DMF, which acted as a solvent and a mild reducing agent (Fig. 1a).[13] As a result, 14 Ag^+ were integrated into **Ag16** through the partial reduction of Ag^+ to Ag^0, leading to the creation of the $\{Ag_{30}\}^{22+}$ nanocluster. We hypothesized that the electronic state of the Ag nanoclusters within **P8W48** could be further modulated using a strong reducing reagent. Upon addition of $TBABH_4$ to the reaction solution of **Ag16** and silver acetate (Fig. S1b; see ESI for details), the color of the solution rapidly shifted from light yellow to dark brown. The UV–vis spectrum of **Ag30** in acetonitrile displayed no characteristic absorption in the visible light region. In contrast, the reaction solution exhibited an absorption band at 472 nm (Fig. S2a), indicating the formation of Ag nanoclusters with distinct structures and/or electronic states, which are different from those of **Ag30**. The introduction of ethyl acetate into the reaction solution produced dark brown block-shaped single crystals (**II**). Notably, the UV–vis spectrum of these crystals dissolved in acetonitrile showed no significant difference from that of the reaction solution, suggesting that **II** was the main product of the reaction (Fig. S2b).

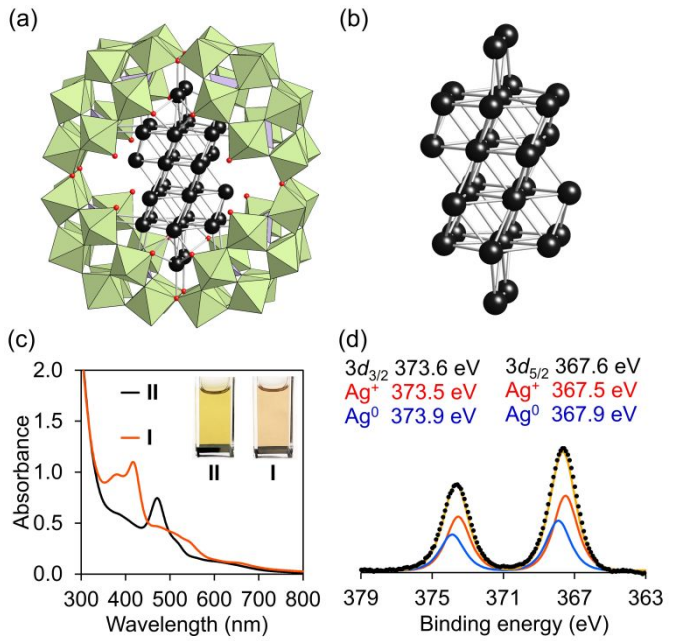

Fig. 2 (a) Crystal structure depicting the anion part of **II**. Green octahedra, $\{WO_6\}$; purple tetrahedra, $\{PO_4\}$; black spheres, Ag atoms; red spheres, O atoms. (b) Structure of an $\{Ag_{30}\}^{18+}$ nanocluster in **II**. (c) UV–vis spectra of **I** and **II** in acetonitrile (10 μM, 1 cm quartz cell). (d) XPS spectrum in the Ag 3*d* region of **II** (black dots) and the sum of the curve-fitting analysis (orange line) obtained through the linear combination of Ag^0 (blue line) and Ag^+ (red line) with an area ratio of Ag^0/Ag^+ = 12/18.

Elemental analysis and acid–base titration (Fig. S3) revealed that the formula of **II** was $TBA_{17}H_5[Ag_{30}P_8W_{48}O_{184}]$, indicating the involvement of 30 Ag atoms within **P8W48**. Single-crystal X-ray structure analysis of **II** (Table S1, Fig. S4) showed distinct electron densities attributed to Ag atoms confined exclusively within the **P8W48** cavity, resulting in the formation of an Ag_{30} nanocluster (Figs. 2a, 2b, and S5). In the crystal structure of **II**, 26 of the 30 Ag atoms were arranged in the fcc structure, while the remaining 4 Ag atoms were integrated into two hinge sites between adjacent $\{P_2W_{12}\}$ units. The Ag_{30} nanocluster in **II** exhibited structural similarity to that of **I** (Tables S2, S3, Fig. S5). The bond valence sum values of P and W indicate the oxidation states of +5 and +6, respectively (Table S4). The UV–vis spectrum of **II** did not show strong absorption in the 600–800 nm range associated with W^{6+}/W^{5+} intervalence charge transfer, indicating that W^{6+} maintained its oxidation state without being reduced to W^{5+} (Fig. 2c).

Although **I** and **II** exhibited similar structures, the UV–vis spectrum of **II** significantly differed from that of **I** (Fig. 2c). Considering that the absorption bands of **I** in the visible light region were attributed to charge transfer from the $\{Ag_{30}\}^{16+}$ nanocluster to the W atoms of **P8W48**, as well as intra-electron excitation within the $\{Ag_{30}\}^{16+}$ nanocluster,[13] this result suggests that **II** possesses a distinct electronic state compared to **I**. Considering the anion charge of **P8W48** ($[P_8W_{48}O_{184}]^{40-}$) and the number of cations (17 TBA^+ and 5 H^+), the charge of the Ag_{30} nanocluster in **II** was determined to be +18. Analysis of the X-ray photoelectron spectroscopy (XPS) spectrum of **II** in the Ag 3d region revealed two peaks at 367.6 eV (Ag $3d_{5/2}$) and 373.6 eV (Ag $3d_{3/2}$) (Fig. 2d). Through curve-fitting analysis, these peaks were deconvoluted into Ag^+ ($3d_{5/2}$ 367.5 eV; $3d_{3/2}$ 373.5 eV) and Ag^0 ($3d_{5/2}$ 367.9 eV, $3d_{3/2}$ 373.9 eV) with an area ratio of Ag^0/Ag^+ = 12/18 (Table S5). These findings confirm the oxidation state of the $\{Ag_{30}\}^{18+}$ nanocluster in **II**, possessing 12 valence electrons, contrasting with the $\{Ag_{30}\}^{16+}$ nanocluster in **I**, which has 14 valence electrons. To further elucidate the electronic state of the Ag_{30} nanocluster in **II**, we conducted solid-state Ag K-edge X-ray absorption fine structure (XAFS) spectroscopy measurements (Fig. 3). The X-ray absorption near-edge structure (XANES) spectrum of **II** was found to be more similar to that of **I** ($\{Ag_{30}\}^{16+}$) than **Ag30** ($\{Ag_{30}\}^{22+}$), corroborating the oxidation state of the $\{Ag_{30}\}^{18+}$ nanocluster in **II** (Figs. 3a, 3b). Additionally, with the introduction of $TBABH_4$ into the acetonitrile solution of **II**, the UV–vis spectrum showed increased absorption bands around 420 and 380 nm, similar to those of **I**, suggesting the conversion of **II** into **I** through further reduction (Fig. S6). This finding further validates the successful synthesis of $\{Ag_{30}\}^{18+}$ nanoclusters, which possess fewer valence electrons than the $\{Ag_{30}\}^{16+}$ nanoclusters in **I**. Overall, we demonstrated the controllable modulation of the oxidation state and structure of Ag_{30} nanoclusters within **P8W48** by selecting appropriate reducing reagents. Although there have been instances of Au or Au-metal alloy nanoclusters displaying multiple oxidation states,[2,16] a pair of Ag nanoclusters sharing similar structures yet differing in oxidation states remains uncommon, largely owing to the inherent instability of Ag nanoclusters, which readily undergo structural change during the modification of oxidation states.[17]

The structure of the Ag_{30} nanocluster in **II** was further investigated using Ag K-edge extended X-ray absorption fine structure (EXAFS) analysis. The *k*-space EXAFS of **II** displayed an oscillation pattern similar to that of **I** (Fig. 3c), aligned with the crystallographic analysis, which revealed no significant structural disparities between the Ag_{30} nanoclusters in **I** and **II**. Conversely, the Fourier-transformed *R*-space EXAFS spectrum of **II** (Fig. 3d) exhibited an intense peak at a slightly longer *R* value than that of **I**, underscoring the structural differentiation between **I** and **II**. Curve-fitting analysis was conducted for the EXAFS spectra of **I** and **II** to elucidate the variance in the Ag–Ag bond length distribution between **I** and **II**, stemming from the subtle displacements of the Ag sites. The coordination number (CN) and Ag–Ag distance (*R*) of **II** (CN = 4.9 ± 0.3, *R* = 2.81 ± 0.03 Å) exceeded those of **I** (CN = 3.9 ± 0.3, *R* = 2.77 ± 0.03 Å) (Table S6). This fitting analysis result was consistent with the expected CN and *R* values derived from crystallographic analysis (CN = 5.0, *R* = 2.82 Å), calculated based on the count and average bond length of Ag–Ag bonds below 2.88 Å. Conversely, EXAFS analysis did not reveal relatively long Ag–Ag bonds (> 2.88 Å), likely owing to interference from a broad bond length distribution. Thus, the fitting analysis of EXAFS, which indicated a larger CN for **II** than for **I**, demonstrated that the $\{Ag_{30}\}^{18+}$ nanocluster in **II** had a shorter Ag–Ag bond (< 2.88 Å) than the $\{Ag_{30}\}^{16+}$ nanocluster in **I**.

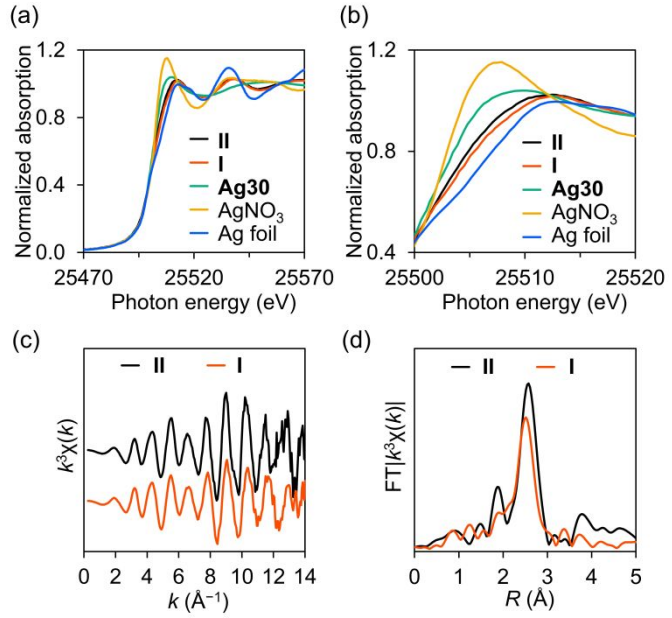

Fig. 3 Solid-state Ag K-edge XAFS measurements of **II** and **I** performed at −263°C. (a) Wide view and (b) enlarged view around the white line (*E* = ca. 25512 eV) of XANES spectra. (c) k^3-weighted *k*-space EXAFS spectra and (d) Fourier-transformed *R*-space EXAFS spectra (*k* range, 3–16 Å).

We then attempted to manipulate the charge distribution in the Ag_{30} nanocluster by protonation and deprotonation of the **P8W48** framework. Given the ability of POMs to reversibly store and release multiple protons in their frameworks owing to their unique acid–base properties, the negative charges of POM ligands can be adjusted by varying the number of protons on the POMs. Exploiting this characteristic, we recently demonstrated that electron donation from the $[Si_2W_{18}O_{66}]^{16-}$ anion to the $\{Ag_{27}\}^{17+}$ nanocluster could be controlled by protonation and deprotonation of the $[Si_2W_{18}O_{66}]^{16-}$ anion.[12d] When *p*-toluenesulfonic acid (TsOH, 0–4 equivalents relative to **II**) was added to the acetonitrile solution of **II**, the UV–vis spectra showed a slight increase in absorbance at λ = 472 nm and decrease at λ = 510 nm (Figs. 4a, S7). This result suggests that the electronic state of **II** can be adjusted by the addition of stoichiometric amounts of TsOH. Moreover, adding TsOH (8–12 equivalents relative to **II**) reduced the absorbance at λ = 472 nm. After the reaction of **II** with TsOH, excess diethyl ether was added to isolate the product as a powder, and the peaks assignable to the C–H vibration of TBA cations (2800–3050 cm^{-1}) were significantly decreased in the IR spectrum (Fig. S8), indicating that the TBA cations of **II** were exchanged with protons upon the reaction with TsOH. On the other hands, when Na^+ ions (sodium trifluoromethanesulfonate) were added to the acetonitrile solution of **II** instead of protons, no significant change was observed in the UV-vis spectra (Fig. S9). These findings imply that the structure and/or electronic state of the Ag nanocluster in **P8W48** was changed by reacting with TsOH.

To further elucidate the structure and electronic state of the Ag_{30} nanocluster in **II** during the reaction with TsOH, solution-state Ag K-edge XAFS studies were performed. The XANES spectra and *k*-space EXAFS oscillation patterns of **II** showed no significant difference between the solid-state and acetonitrile solutions, indicating that the structure and electronic state of the Ag_{30} nanocluster in **II** remained unchanged in solution (Fig. S10). Moreover, both the *k*-space and Fourier-transformed *R*-space EXAFS spectra of the reaction solution of **II** and TsOH showed no significant changes, indicating the structural integrity of the Ag_{30} nanocluster in **II** during the reaction (Figs. S11 and S12). However, the XANES spectra of the reaction solution containing **II** and TsOH revealed an increasing white line (*E* = ca. 25512 eV) as the amount of TsOH increased (Figs. 4b, S13a, and S13b). This result suggests that the protonation of **II** reduces electron donation from the **P8W48** ligand to the Ag_{30} nanocluster, resulting in changes in the UV–vis absorption. Furthermore, upon the addition of an equivalent amount of TBAOH relative to TsOH to the reaction solution of **II** and TsOH, the UV–vis and XANES spectra reverted to characteristics resembling those of the original **II**, indicating that the electronic state of the Ag_{30} nanocluster in **II** can be controlled by adding stoichiometric amounts of acid and base (Figs. S14, S15a, and S15b).

Finally, density functional theory calculations were performed to analyze the natural charge population of the $\{Ag_{30}\}^{18+}$ nanocluster in **II**, considering different numbers of protons on the **P8W48** ligand (see experimental details in the ESI; Fig. S16). The calculation with four protons on the $[\{Ag_{30}\}^{18+}P_8W_{48}O_{184}]^{22-}$ anion showed that the natural charges of the Ag atoms at the center of the Ag_{30} nanocluster (i.e., Ag4, Ag6, and Ag7; Figs 4c, S17, Tables S7) ranged from −0.33 to −0.16, which were more negative than those of the other Ag atoms on the surface or adjacent to the **P8W48** ligand (i.e., 0.46–0.81 for Ag1, Ag2, Ag3, Ag5, and Ag8). The total natural charge of the Ag_{30} nanoclusters within the ring-shaped POM (i.e., $[H_4P_8W_{48}O_{184}]^{36-}$) was +11.3, which is more negative than that of the Ag_{30} nanocluster without the POM ligand (+18.0) (Fig. S18). This suggests that the POM ligand acts as an electron-donating ligand. The total natural charges of the Ag_{30} nanocluster with 4, 8, and 12 protons on the **P8W48** ligand were +11.3, +11.6, and +11.8, respectively, indicating a decrease in the electron density of the Ag_{30} nanocluster with an increase in the number of protons on the **P8W48** ligand. This observation aligns with the results of the Ag K-edge XANES analysis. With an increase in the number of protons on the **P8W48** ligand from 4 to 8 (i.e., $[H_4P_8W_{48}O_{184}]^{36-}$ to $[H_8P_8W_{48}O_{184}]^{32-}$), the natural charge of Ag4 became more negative, whereas those of Ag7 became more positive (Fig. 4c). However, with the addition of 4 more protons (forming $[H_{12}P_8W_{48}O_{184}]^{28-}$), the natural charge of Ag4 became more positive and that of Ag7 became more negative. Additionally, the Ag3, Ag4, and Ag6 sites showed a slight increase in natural charge by 0.02–0.04, indicating a reduction in electron donation from the **P8W48** ligand, influencing the electronic state of the Ag_{30} nanocluster within **P8W48**. These findings suggest that the charge distribution of Ag nanoclusters can be controlled by the protonation states of the POM ligands. Additionally, given that the changes in the natural charge populations exhibited different trends depending on the number of protons, this computational study aligns with the multistep changes observed in the UV–vis spectra of the reaction solution when **II** was reacted with increasing amounts of TsOH. These results suggested that the positions of protons

added to **P8W48** differ every 4 equivalents, resulting in a significant change in the UV-Vis spectra of **II** with the addition of 4, 8, and 12 equivalents of TsOH (Fig. S16).

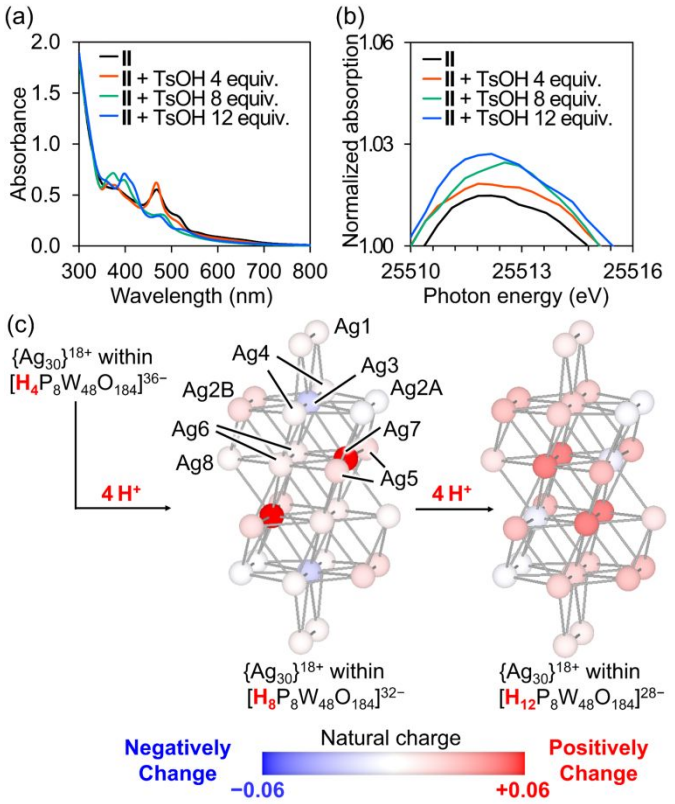

Fig. 4 (a) UV–vis spectra of **II** after adding TsOH (4, 8, and 12 equivalents) in acetonitrile. (b) The enlarged view around the white line (E = ca. 25512 eV) of solution-state Ag K-edge XANES spectra of **II** upon TsOH addition in acetonitrile. (c) Changes in the natural charge of the $\{Ag_{30}\}^{18+}$ nanocluster within a ring-shaped POM upon protonation. Change in the natural charge of each Ag atom after adding protons to a ring-shaped POM framework. Ag atoms are color-coded based on the changes in the natural charges.

Conclusions

In this study, we demonstrated the modulation of the electronic state of Ag_{30} nanoclusters within a ring-shaped POM ($[P_8W_{48}O_{184}]^{40-}$, denoted as **P8W48**) using two approaches. An $\{Ag_{30}\}^{18+}$ nanocluster in **P8W48** was synthesized by adding tetra-*n*-butylammonium borohydride as a reducing reagent to a reaction solution of 16 Ag^+-containing **P8W48** and Ag^+ ions. The $\{Ag_{30}\}^{18+}$ nanocluster in **P8W48** possessed an fcc-type structure similar to that of the previously reported $\{Ag_{30}\}^{16+}$ nanocluster[13] despite the different oxidation states. Moreover, we demonstrated that the charge distribution of the $\{Ag_{30}\}^{18+}$ nanocluster could be modulated by leveraging the acid–base properties of the POMs. These findings suggest that POM-stabilized Ag nanoclusters with different structures and electronic states can be obtained by controlling the synthetic conditions and post-synthetic modulation. This capability will accelerate the development of their applications and properties, including their catalytic activity, photochemical properties, adsorption, sensing, and medical applications.

Conflicts of interest

There are no conflicts to declare.

Data availability

The data supporting this manuscript is available in the ESI† of and available on request. Crystallographic data for **II** has been deposited at the CCDC (deposition number 2361048) and can be obtained free of charge from Cambridge Crystallographic Data Centre via www.ccdc.cam.ac.uk/data_request/cif.

Acknowledgements

This work was supported by JST FOREST (JPMJFR213M), JST SPRING (JPMJSP2108), and JSPS KAKENHI (22H04971, 24H02210, 24H02217). XAFS measurements at SPring-8 were conducted with the approval of the Japan Synchrotron Radiation Research Institute (proposal numbers 2023B1651, 2023B2070). Single-crystal X-ray diffraction measurements at SPring-8 were conducted with the approval of the Japan Synchrotron Radiation Research Institute (proposal numbers 2023B1842, 2023A1731). A part of computations was performed using Research Center for Computational Science, Okazaki, Japan (Project: 23-IMS-C106, 24-IMS-C101).

References

1 (*a*) I. Chakraborty and T. Pradeep, *Chem. Rev.*, 2017, **117**, 8208–8271; (*b*) Y. Du, H. Sheng, D. Astruc and M. Zhu, *Chem. Rev.*, 2020, **120**, 526–622; (*c*) G.-G. Luo, Q.-L. Guo, Z. Wang, C.-F. Sun, J.-Q. Lin and D. Sun, *Dalton Trans.*, 2020, **49**, 5406–5415; (*d*) S. Takano and T. Tsukuda, *J. Am. Chem. Soc.*, 2021, **143**, 1683–1698; (*e*) M. F. Matus and H. Häkkinen, *Nat. Rev. Mater.*, 2023, **8**, 372–389.

2 (*a*) Y. Negishi, N. K. Chaki, Y. Shichibu, R. L. Whetten and T. Tsukuda, *J. Am. Chem. Soc.*, 2007, **129**, 11322–11323; (*b*) M. Zhu, W. T. Eckenhoff, T. Pintauer and R. Jin, *J. Phys. Chem. C* 2008, **112**, 14221–14224; (*c*) M. A. Tofanelli, K. Salorinne, T. W. Ni, S. Malola, B. Newell, B. Phillips, H. Häkkinen and C. J. Ackerson, *Chem. Sci.*, 2016, **7**, 1882–1890.

3 (*a*) M. A. Tofanelli and C. J. Ackerson, *J. Am. Chem. Soc.*, 2012, **134**, 16937–16940; (*b*) C. B. Collins, M. A. Tofanelli, M. F. Crook, B. D. Phillips and C. J. Ackerson, *RSC Adv.*, 2017, **7**, 45061–45065.

4 (*a*) M. Zhu, C. M. Aikens, M. P. Hendrich, R. Gupta, H. Qian, G. C. Schatz and R. Jin, *J. Am. Chem. Soc.*, 2009, **131**, 2490–2492; (*b*) S. Antonello, N. V. Perera, M. Ruzzi, J. A. Gascón and F. Maran, *J. Am. Chem. Soc.*, 2013, **135**, 15585–15594.

5 (*a*) R. J.-Mosqueda and G. Mpourmpakis, *Phys. Chem. Chem. Phys.*, 2019, **21**, 22272–22282; (*b*) K. Kwak, Q. Tang, M. Kim, D.-e. Jiang and D. Lee, *J. Am. Chem. Soc.*, 2015, **137**, 10833–10840.

6 (*a*) D. R. Kauffman, D. Alfonso, C. Matranga, P. Ohodnicki, X. Deng, R. C. Siva, C. Zeng and R Jin, *Chem. Sci.*, 2014, **5**, 3151–3157; (*b*) G. Li, W. Hu, Y. Sun, J. Xu, X. Cai, X. Cheng, Y. Zhang, A. Tang, X. Liu, M. Chen, W. Ding and Y. Zhu, *Angew. Chem.,*

Int. Ed., 2020, **59**, 21135–21142; (*c*) H. Chong, P. Li, S. Wang, F. Fu, J. Xiang, M. Zhu and Y. Li, *Sci. Rep.*, 2013, **3**, 3214.

7 (*a*) Z. Liu, H. Tan, B. Li, Z. Hu, D.-e. Jiang, Q. Yao, L. Wang and J. Xie, *Nat. Commun.*, 2023, **14**, 3374; (*b*) Z. Wu and R. Jin, *Nano Lett.*, 2010, **10**, 2568–2573; (*c*) A. Cirri, H. M. Hernández, C. Kmiotek and C. J. Johnson, *Angew. Chem., Int. Ed.*, 2019, **58**, 13818–13822.

8 (*a*) Z.-J. Guan, R.-L. He, S.-F. Yuan, J.-J. Li, F. Hu, C.-Y. Liu and Q.-M. Wang, *Angew. Chem., Int. Ed.*, 2022, **61**, e202116965; (b) Y. Zeng, S. Havenridge, M. Gharib, A. Baksi, K. L. D. M. Weerawardene, A. R. Ziefuß, C. Strelow, C. Rehbock, A. Mews, S. Barcikowski, M. M. Kappes, W. J. Parak, C. M. Aikens and I. Chakraborty, *J. Am. Chem. Soc.*, 2021, **143**, 9405–9414.

9 (*a*) M. T. Pope, *Heteropoly and Isopoly Oxometalates*, Springer, Berlin, 1983; (*b*) C. L. Hill and C. M. Prosser-McCartha, *Coord. Chem. Rev.*, 1995, **143**, 407–455; (*c*) H. N. Miras, J. Yan, D.-L. Long and L. Cronin, *Chem. Soc. Rev.*, 2012, **41**, 7403–7430; (*d*) S.-S. Wang and G.-Y. Yang, *Chem. Rev.*, 2015, **115**, 4893–4962; (*e*) I. A. Weinstock, R. E. Schreiber and R. Neumann, *Chem. Rev.,* 2018, **118**, 2680–2717; (*f*) K. Suzuki, N. Mizuno and K. Yamaguchi, *ACS Catal.*, 2018, **8**, 10809–10825; (*g*) N. I. Gumerova and A. Rompel, *Nat. Rev. Chem.*, 2018, **2**, 0112; (*h*) A. Misra, K. Kozma, C. Streb and M. Nyman, *Angew. Chem.*, *Int. Ed.*, 2020, **59**, 596–612; (*i*) J.-H. Kruse, M. Langer, I. Romanenko, I. Trentin, D. Hernández-Castillo, L. González, F. H. Schacher and C. Streb, *Adv. Funct. Mater.*, 2022, **32**, 2208428.

10 (*a*) K. Zhou, C. Qin, H.-B. Li, L.-K. Yan, X.-L. Wang, G.-G. Shan, Z.-M. Su, C. Xu and X.-L. Wang, *Chem. Commun.*, 2012, **48**, 5844–5846; (*b*) Z. Wang, H.-F. Su, C.-H. Tung, D. Sun and L.-S Zheng. *Nat. Commun.,* 2018, **9**, 4407; (*c*) H. Liu, C.-Y. Song, R.-W. Huang, Y. Zhang, H. Xu, M.-J. Li, S.-Q. Zang and G.-G. Gao, *Angew. Chem., Int. Ed.* 2016, **55**, 3699–3703; (*d*) Y.-M. Su, Z. Wang, G.-L. Zhuang, Q.-Q. Zhao, X.-P. Wang, C.-H. Tunga and D. Sun, *Chem. Sci.*, 2019, **10**, 564–568; (e) Z. Zhao, M. Zhao, L. Deng, Q. Li, J. Zhang, H. Su, H. Lv and G.-Y. Yang, *Chem. Commun.*, 2024, **60**, 5415–5418.

11 (*a*) K.-G. Liu, X.-Y. Liu, Z.-J. Guan, K. Shi, Y.-M. Lin and Q.-M. Wang, *Chem. Commun.*, 2016, **52**, 3801–3804; (*b*) S. Tamari, K. Ono, M. Hashimoto and T. Ozeki, *Dalton Trans.*, 2015, **44**, 19056–19058; (*c*) F. Gruber and M. Jansen, *Angew. Chem., Int. Ed.*, 2010, **49**, 4924–4926; (*d*) G.-G. Gao, P.-S. Cheng and T. C. W. Mak, *J. Am. Chem. Soc.* 2009, **131**, 18257–18259; (*e*) X. Fan, F. Yuan, D. Li, S. Chen, Z. Cheng, Z. Zhang, S. Xiang, S.-Q. Zang, J. Zhang and Lei Zhang, *Angew. Chem., Int. Ed.*, 2021, **60**, 12949 –12954; (*f*) X. Fan, S. Chen, L. Zhang and J. Zhang, *Chem. Eur. J.*, 2021, **27**, 15563–15570.

12 (*a*) K. Yonesato, H. Ito, H. Itakura, D. Yokogawa, T. Kikuchi, N. Mizuno, K. Yamaguchi and K. Suzuki, *J. Am. Chem. Soc.*, 2019, **141**, 19550–19554; (*b*) K. Yonesato, H. Ito, D. Yokogawa, K. Yamaguchi and K. Suzuki, *Angew. Chem., Int. Ed.*, 2020, **59**, 16361–16365; (*c*) K. Yonesato, S. Yamazoe, D. Yokogawa, K. Yamaguchi and K. Suzuki, *Angew. Chem., Int. Ed.*, 2021, **60**, 16994–16998; (*d*) K. Yonesato, S. Yamazoe, S. Kikkawa, D. Yokogawa, K. Yamaguchi and K. Suzuki, *Chem. Sci*., 2022, **13**, 5557–5561.

13 K. Yonesato, D. Yanai, S. Yamazoe, D. Yokogawa, T. Kikuchi, K. Yamaguchi and K. Suzuki, *Nat. Chem.*, 2023, **15**, 940–947.

14 (*a*) R. Contant and A. Tézé, *Inorg. Chem.*, 1985, **24**, 4610–4614; (*b*) S. Sasaki, K. Yonesato, N. Mizuno, K. Yamaguchi and K. Suzuki, *Inorg. Chem.*, 2019, **58**, 7722–7729.

15 (*a*) S. S. Mal and U. Kortz, *Angew. Chem.*, *Int. Ed.*, 2005, **44**, 3777–3780; (*b*) S. S. Mal, M. H. Dickman, U. Kortz, A. M. Todea, A. Merca, H. Bögge, T. Glaser, A. Müller, S. Nellutla, N. Kaur, J. van Tol, N. S. Dalal, B. Keita and L. Nadjo, *Chem. Eur. J.*, 2008, **14**, 1186–1195; (*c*) P. Yang, M. Alsufyani, A.-H. Emwas, C. Chen, and N. M. Khashab, *Angew. Chem.*, *Int. Ed.*, 2018, **57**, 13046–13051; (*d*) Y. Koizumi, K. Yonesato, S. Kikkawa, S. Yamazoe, K. Yamaguchi and K. Suzuki, *J. Am. Chem. Soc.*, 2024, **146**, 14610–14619.

16 (*a*) M. Suyama, S. Takano, T. Nakamura and T. Tsukuda, *J. Am. Chem. Soc.*, 2019, **141**, 14048–14051; (*b*) Q. Li, J. Chai, S. Yang, Y. Song, T. Chen, C. Chen, H. Zhang, H. Yu and M. Zhu, *Small*, 2021, **17**, 1907114; (*c*) Y. Song, S. Jin, X. Kang, J. Xiang, H. Deng, H. Yu and M. Zhu, *Chem. Mater.*, 2016, **28**, 2609–2617.

17 (*a*) R. S. Dhayal, Y.-R. Lin, J.-H. Liao, Y.-J. Chen, Y.-C. Liu, M.-H. Chiang, S. Kahlal, J.-Y. Saillard and C. W. Liu, *Chem. Eur. J.*, 2016, **22**, 9943–9947; (*b*) W.-J. Yen, J.-H. Liao, T.-H. Chiu, J.-Y. Chen, Y. J. Chen, S. Kahlal, J.-Y. Saillard and C. W. Liu, *Nanoscale*, 2024, **16**, 7011–7018; (*c*) P.-K. Liao, K.-G. Liu, C.-S. Fang, Y.-Y. Wu and C. W. Liu, *J. Clust. Sci.*, 2019, **30**, 1185–1193.

Data availability

The data supporting this manuscript is available in the ESI† of and available on request. Crystallographic data for **II** has been deposited at the CCDC (deposition number 2361048) and can be obtained free of charge from Cambridge Crystallographic Data Centre via www.ccdc.cam.ac.uk/data_request/cif.